

1           Evolving Sahel rainfall response to  
2 anthropogenic aerosols driven by shifting  
3 regional oceanic and emission influences  
4

5                           Haruki Hirasawa<sup>1\*</sup>, Paul J. Kushner<sup>1</sup>

6                           Michael Sigmond<sup>2</sup>, John Fyfe<sup>2</sup>

7                           Clara Deser<sup>3</sup>  
8

9                   1 Department of Physics, University of Toronto, Toronto, Ontario, Canada.

10                  2 Canadian Centre for Climate Change Modelling and Analysis, Environment and Climate  
11                           Change Canada, Victoria, British Columbia, Canada.

12                  3 National Center for Atmospheric Research, Boulder, Colorado, USA  
13

14                           Corresponding Author E-mail:

15                           hirasawa@physics.utoronto.ca

16

## 17 0.1 Abstract

18 Sahel summertime precipitation declined from the 1950s to 1970s and recovered from the 1970s  
19 to 2000s. Anthropogenic aerosol contributions to this evolution are typically attributed to  
20 interhemispheric gradient changes of Atlantic sea surface temperature (SST). However recent  
21 work by Hirasawa et al., 2020 indicates a more complex picture, with the response being a  
22 combination of “fast” direct-atmospheric (DA) processes and “slow” ocean-mediated (OM)  
23 processes. Here, we extend this understanding using the Community Atmosphere Model 5 to  
24 determine the role of regional ocean-basin perturbations and regional aerosol emission changes  
25 in the overall aerosol-driven OM and DA responses, respectively. From the 1950s to 1970s, there  
26 was an OM Sahel wetting response due to Pacific cooling which was offset by drying due to  
27 Atlantic cooling. By contrast, from the 1970s to 2000s, Atlantic trends reversed and amplified  
28 the Pacific cooling induced wetting. This wetting was partially offset by drying driven by Indian  
29 Ocean cooling. Thus, the OM Sahel precipitation response to aerosol crucially depends on the  
30 balance of responses to Atlantic, Pacific, and Indian Ocean SST anomalies. From the 1950s to  
31 1970s, there is DA Sahel drying that was principally due to North American aerosol emissions,  
32 with negligible effect from European emissions. DA drying from the 1970s to 2000s was mainly  
33 due to African aerosol emissions. Thus, the shifting roles of regional OM and DA effects reveals  
34 a complex interplay of direct driving and remote teleconnections in determining the time  
35 evolution of Sahel precipitation due to aerosol forcing in the late 20<sup>th</sup> century.

## 36 0.2 Significance Statement

37 Studies of global climate models consistently indicate that anthropogenic aerosol emissions were  
38 a significant contributor to a severe drought that occurred in the Sahel region of Africa in the late  
39 20<sup>th</sup> century. The drying influence of aerosol forcing is the combined result of rapid atmospheric  
40 responses directly due to the forcing and slower responses due to forced ocean temperature  
41 changes. Using a set of simulations targeted at determining the influences from different ocean  
42 basins and different emission regions for two periods in the late 20<sup>th</sup> century, we find there is a  
43 surprising range of mechanisms through which aerosol emissions affect the Sahel. This results in  
44 a complex interplay of at times competing and at times complementary regional influences.

## 45 1. Introduction

46 The influence of external forcing on climate variability in the Sahel region of Africa has been  
47 extensively studied, with much attention focused on understanding the drivers of the drought that  
48 afflicted the region with its peak in the 1970s and 1980s. Much of the variability is understood to  
49 be linked to global sea surface temperature (SST) variability, which is in large part internal  
50 (Folland et al. 1986; Rodríguez-Fonseca et al. 2011; Biasutti et al. 2008; Biasutti 2019).  
51 However, an array of studies using coupled global climate model (GCM) simulations have  
52 identified anthropogenic sulfate aerosol forcing as a significant driver of drought in the Sahel  
53 (Rotstayn and Lohmann 2002; Held et al. 2005; Kawase et al. 2010; Ackerley et al. 2011;  
54 Westervelt et al. 2017; Undorf et al. 2018; Hua et al. 2019; Giannini and Kaplan 2019; Herman  
55 et al. 2020). Aerosol and their precursor emissions have undergone substantial and spatially  
56 varied changes on multidecadal timescales. In particular, sulfur dioxide, the precursor chemical  
57 to sulphate aerosol, is characterized by an initial increasing trend up to the 1970s focused in  
58 North American and Europe and decreases in these regions after the 1970s along with strong  
59 increases in South and East Asia (Smith et al. 2011). The timing and spatial pattern of these  
60 aerosol changes results in multidecadal changes in Sahel climate that can be identified in single  
61 forcing GCM simulations for which there is a sufficient ensemble size to filter internal variability  
62 (Hua et al. 2019; Deser et al. 2020).

63 In the National Center for Atmospheric Research (NCAR) Community Earth System Model  
64 1 (CESM1) Large ensemble (LE) single forcing simulations (Deser et al. 2020), it is found that  
65 aerosol forcing reduced July-August-September (JAS) precipitation in the Sahel for the 1970s  
66 minus 1950s (Fig. 1a) and increased precipitation for the 2000s minus 1970s (Fig. 1b). This  
67 aerosol forcing effect is the dominant driver of historical multidecadal Sahel precipitation  
68 variability in CESM1 (Hirasawa et al. 2020). GHG forcing has little contribution to the 1970s  
69 minus 1950s change but contributes to the recovery from the 1970s onwards. The CESM1 LE  
70 ensemble mean multidecadal variability in Sahel rainfall is similar in timing to the observed  
71 variability. However, both the ensemble mean and spread are substantially smaller in magnitude  
72 compared to observed variability (Hirasawa et al. 2020), which is a common problem in coupled  
73 GCMs (Biasutti 2013; Undorf et al. 2018). Such aerosol-induced impacts are typically  
74 interpreted as a response to hemispheric asymmetries in Atlantic SST anomalies caused by

75 regional emission changes in North America and Europe. These hemispheric asymmetries drive  
 76 shifts in the Atlantic intertropical convergence zone (ITCZ) and West African monsoon  
 77 southward, drying the Sahel (Ackerley et al. 2011; Mohino et al. 2011; Hwang et al. 2013; Wang  
 78 2015; Hua et al. 2019). Such an interhemispheric SST anomaly pattern is also seen in the  
 79 CESM1 LE aerosol forcing effect. In these simulations the sign of the interhemispheric Atlantic  
 80 SST contrast anomaly switches between the 1970s minus 1950s epoch difference (Fig. 1a over  
 81 ocean) to the 2000s minus 1970s epoch difference (Fig. 1b over ocean). Thus, one might

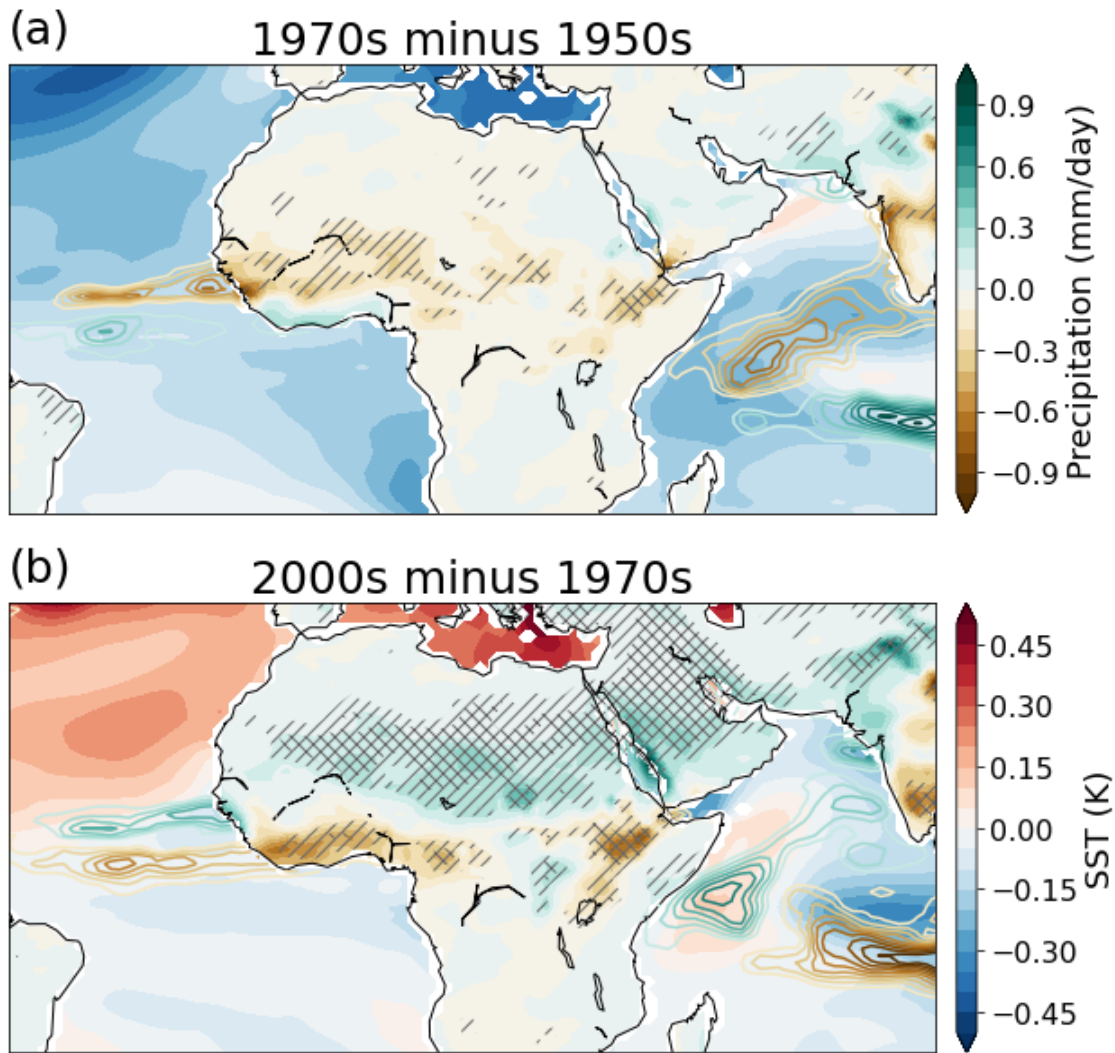


Figure 1: JAS Precipitation anomalies over land and JAS SST anomalies over ocean in filled contours from the CESM1 LE All minus All-but-industrial aerosol forcing simulations for the 1970s minus 1950s (a) and 2000s minus 1970s (b). Precipitation anomalies over ocean are shown using contours with the same color-bar as the land precipitation but excluding the zero contour. Signals that pass a Student's t-test at the 95% level are single hatched in grey, while signals that additionally pass the False Detection Rate (FDR) test are cross hatched ( $p_{FDR} = 2.5 \times 10^{-3}$ ).

82 interpret the Sahel precipitation change seen in CESM1 as the result of this Atlantic hemispheric  
83 SST asymmetry mechanism.

84 However, forcing can directly cause changes in the atmosphere even in the absence of SST  
85 changes. For example, surface albedo reductions cause subsidence and thus drying in the Sahel  
86 (Charney 1975; Pausata et al. 2016; Gaetani et al. 2017). Aerosol forcing can have a similar  
87 effect, with local increases in shortwave reflectance reducing precipitation, as well as through the  
88 effect of remote aerosol changes in regions like Asia have via atmospheric teleconnections  
89 (Dong et al. 2014; Dong and Sutton 2015; Liu et al. 2018; Hirasawa et al., 2020). Furthermore,  
90 independent of aerosol forcing, SST anomalies in the tropical Pacific Ocean caused by El Niño  
91 or greenhouse gas warming have substantial effects on Sahel climate, by warming the tropical  
92 upper troposphere over the Sahel, which increases the threshold for convection and reduces  
93 precipitation (Rowell 2001; Giannini et al. 2008; Giannini and Kaplan 2019). Indian Ocean  
94 warming and increasing north-south SST gradients also have a drying effect on the Sahel (Chung  
95 and Ramanathan 2006; Lu 2009; Dyer et al. 2017). We therefore expect aerosol-forced cooling  
96 will have similar, opposite sign effects to these warming effects. Thus, it is difficult to parse the  
97 pathways through which aerosol forcing influences the climate using coupled GCM experiments  
98 alone and the aerosol impact on the Sahel is influenced by a range of factors other than the North  
99 Atlantic SST change.

100 In our previous work (Hirasawa et al., 2020 - H2020), we used two coupled model Large  
101 Ensembles (CESM1 and Environment and Climate Change Canada's Canadian Earth System  
102 Model 2; CanESM2) and their respective atmosphere-land components (Canadian Atmosphere  
103 Model 4 (CanAM4) and Community Atmosphere Model 5 (CAM5) respectively) to separately  
104 identify the direct-atmospheric (DA) effect of aerosol forcing due to rapid adjustments of the  
105 atmosphere and land and the slower ocean-mediated (OM) effect due to aerosol forced SST  
106 changes. The two epochs shown in Fig. 1, the 1970s minus 1950s (early period) and the 2000s  
107 minus 1970s (late period), were examined with a suite of atmosphere-land GCM experiments. It  
108 was found that the DA effect caused JAS drying in both periods, similar to that found in Dong et  
109 al. (2015). On the other hand, the OM effect resulted in a JAS precipitation increase in the early  
110 period despite cooling of the North Atlantic relative to the South Atlantic in these experiments.  
111 In the late period, the OM effect caused additional increases in JAS Sahel precipitation. Thus, the

112 early period drying in the coupled model response was predominantly DA, while the late period  
113 recovery was predominantly OM in these models. Though there were differences in the pattern  
114 and magnitude of the response, the relative roles of the DA and OM effects were qualitatively  
115 similar in the CanAM4 and CAM5.

116 This work seeks to extend the analysis of H2020 in order to understand the mechanisms  
117 underlying the OM and DA effects documented therein. Focusing on the NCAR CAM5 model,  
118 we use additional simulations to decompose the OM and DA effects into their regional  
119 components by applying SST anomalies in different ocean basins individually for the OM effect  
120 and emission changes in different regions individually for the DA effect. In the case of the OM  
121 effect, the basin-level decomposition was motivated by the wetting response seen in the early  
122 period, which was hypothesized to be a result of the effect of North Atlantic cooling being offset  
123 by a reverse “upped-ante” effect due to tropical SST cooling (Chou and Neelin 2004; Giannini et  
124 al. 2013; Giannini and Kaplan 2019). In the case of the DA effect, the regional emission  
125 decomposition was motivated by the persistence of a DA drying signal in the late period, despite  
126 large declines in sulphate concentrations over North Africa due to declining European emissions.  
127 This drying signal was hypothesized to be a teleconnected response to increasing Asian  
128 emissions (Dong et al. 2014; Liu et al. 2018).

129 The experiments used here are similar to those conducted for the Precipitation Driver  
130 Response Model Intercomparison Project (PDRMIP) in which large, idealized aerosol  
131 perturbations are applied regionally to coupled GCM and AGCMs (Myhre et al. 2017; Liu et al.  
132 2018). Liu et al. (2018) found that a large increase in Asian sulphate (black carbon) emissions  
133 caused annual-mean wetting (drying) in the Sahel that is in largely DA driven, while increasing  
134 European sulphate emissions cause principally OM-driven drying. In this work, we instead study  
135 the decomposition of DA and OM effects for two periods characterizing first the general rise in  
136 emissions focused in North America and Europe and then the west-to-east geographic shift of  
137 aerosol emissions. The differing impact of historical aerosol forcing in these two periods has  
138 gained increasing interest in recent studies, as the short atmospheric lifetime of aerosols results  
139 in differing patterns of aerosol forcing and climate response (Wang 2015; Deser et al. 2020;  
140 Kang et al. 2021). Furthermore, we explicitly determine the OM effect by conducting AGCM  
141 experiments using aerosol-forced SST perturbations derived from a large ensemble of coupled

142 GCM simulations, rather than as the residual between the coupled GCM and AGCM simulations  
143 as in PDRMIP (Liu et al. 2018).

144 In section 2, we describe the CESM1 LE and CAM5 simulations used in this analysis. In  
145 sections 3 and 4, we discuss the effect of regional SST and regional emission perturbations on  
146 the Sahel, respectively, and discuss the mechanisms underlying these responses. In section 5, we  
147 discuss the additivity of response to regional SST and regional emission perturbations. In section  
148 6, we summarize our results and make concluding remarks.

## 149 2. Methods

150 The role of the OM and DA effects on the Sahel are determined using a set of prescribed-  
151 SST simulations conducted with the NCAR – Department of Energy Community Atmosphere  
152 Model version 5 (CAM5) (Neale et al. 2012). CAM5 includes basic chemistry and represents  
153 aerosols using a three Mode Aerosol Model (MAM3) (Liu et al. 2012). Thus, aerosols are  
154 prescribed via specification of emissions of aerosols and aerosol precursor chemicals.  
155 Furthermore, CAM5 includes representation of aerosol-cloud interactions including the cloud  
156 albedo and lifetime effects (Neale et al. 2012). These result in a total effective radiative forcing  
157 of  $-1.37\text{Wm}^{-2}$  by the early 21st century which is relatively strong among CMIP5 models  
158 (Zelinka et al. 2014). CAM5 overestimates the enhancement of cloud liquid water path in  
159 response to aerosol perturbations from tropospheric volcanic aerosols, which may result in an  
160 overestimation of the aerosol-cloud lifetime effect (Malavelle et al. 2017; Toll et al. 2019). The  
161 simulations are carried out at a nominal  $1^\circ$  resolution.

162 Here we use so-called “time-slice” simulations, which have atmospheric boundary  
163 conditions that vary seasonally but are fixed year-to-year. The baseline SST and sea ice  
164 concentration (SIC) climatology is the 2000-2009 average of the Hadley Centre Sea Ice and Sea  
165 Surface Temperature (HadISST) data set (Hurrell et al. 2008). Climatological atmosphere and  
166 land composition conditions are taken as the 2000-2009 average, based on historical data for  
167 2000-2005 and RCP8.5 emissions for 2006-2009. The OM effect is determined by perturbing the  
168 climatological SST/SIC with anomalies due to aerosol forcing for the 2000s minus the 1950s or  
169 the 2000s minus the 1970s, while keeping aerosol emissions fixed at climatological values. We  
170 do not modify sea ice thickness in these simulations. The aerosol-forced SST/SIC anomalies are

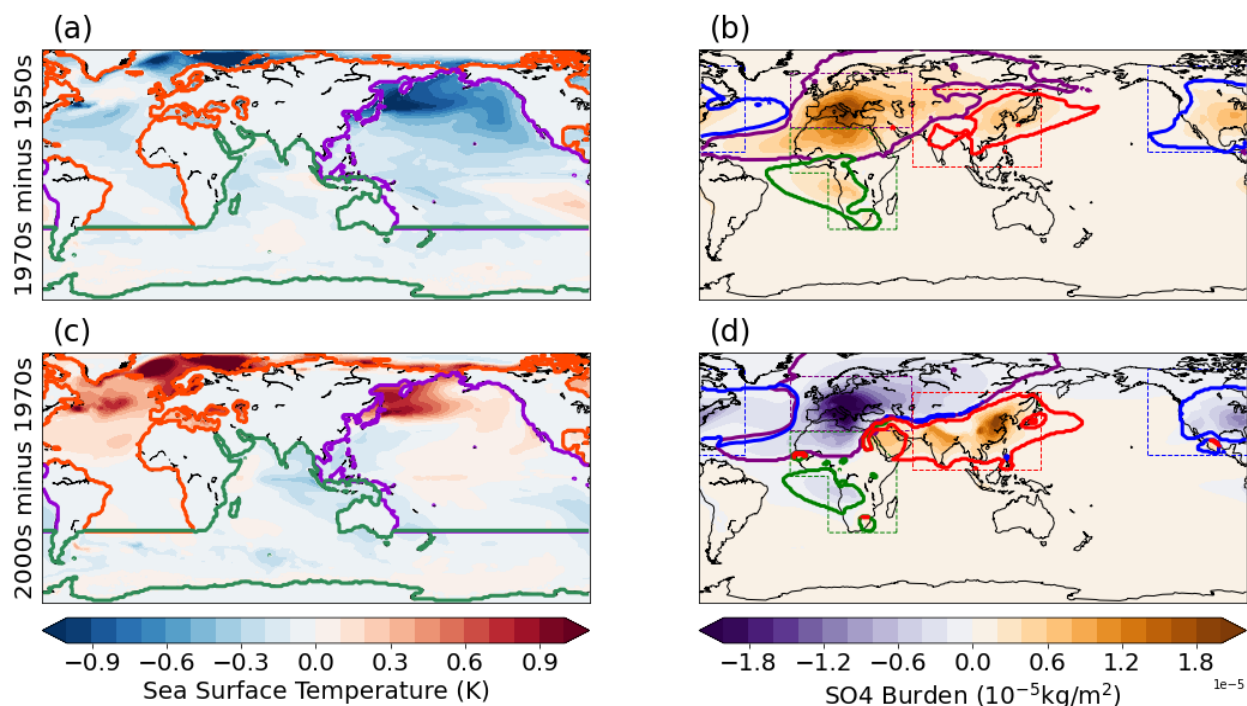


Figure 2: For the 1970s minus 1950s (top - a, b) and 2000s minus 1970s (bottom - c, d), the aerosol-forced JAS Sea Surface Temperature (SST) anomalies (left - a,c) from the CESM1 LE All minus All-but-aerosol simulations and Sulphate (SO4) burden anomalies from the total direct-atmospheric response simulations (right - b,d). In a,c the ocean basins used in the regional ocean-mediated response simulations are outlined in orange (ATL), green (IND), and purple (PAC). In b,d solid contours indicate the regions in which the SO4 burden anomaly for a given regional emissions simulation accounts for more than 50% of the total SO4 burden anomaly and has a magnitude greater than  $10^{-6} \text{ kg/m}^2$ . The geographic region used to define the emissions from a given region are outlined using dashed lines in blue (N AM), purple (EURO), green (AFRI), and red (ASIA). Note we apply the 2000s minus 1970s and 2000s minus 1950s anomalies in the simulations, but show the 1970s minus 1950s anomaly for easier comparison to our results. JAS anomalies are shown for direct comparison of the forcings to the responses in later figures.

171 calculated by taking the difference between the ensemble means of historical “all forcing” (ALL)  
 172 and “all-but-aerosol” (XAER) forcing simulations from the NCAR CESM1-LE (Deser et al.  
 173 2020) (Figs 2a, 2c), then computing the epoch differences. The XAER forcing LE is a 20-  
 174 member initial condition ensemble in which all forcings follow their historical values except for  
 175 industrial aerosols, which are held to 1920 conditions. Further simulations are conducted in  
 176 which the SST/SIC perturbations are only applied in one of a set of three ocean basins: the  
 177 Atlantic Ocean, Arctic Ocean, and Mediterranean Sea (ATL), the Indian and Southern Oceans  
 178 (IND), and the Pacific Ocean (PAC) (coloured contours in Figs. 2a, 2c).

179 The DA effect is determined by modifying emissions of aerosols and their precursor  
 180 chemicals to the target decadal levels, while keeping SST/SIC conditions at 2000s levels

181 (resulting sulphate (SO<sub>4</sub>) and black carbon (BC) burden changes shown in Fig. 2b, 2d and Fig.  
182 S1a, S1b respectively). Further simulations are then conducted in which emissions are only  
183 changed in one of four emission regions: North America (N AM), Europe (EURO), Africa  
184 (AFRI), and Asia (ASIA), the definitions for which are shown using the dashed lines in Fig. 2b  
185 and 2d. Note that we do not include all possible emission regions and have not tested regions  
186 such as the Arabian Peninsula, South America, and Oceania. Nevertheless, the selected emission  
187 regions account for the vast majority of SO<sub>4</sub> and BC burden anomalies (Fig. S2). Over Africa,  
188 there are differences in the SO<sub>4</sub> burden between the global emission change and the sum of the  
189 regional experiments, particularly near the Arabian Peninsula and Europe, but these differences  
190 are not statistically significant. In both DA and OM experiments, we conduct 2000s minus 1970s  
191 and 2000s minus 1950s experiments, with the 1970s minus 1950s response calculated as the  
192 difference of the two. This results in more noise in the 1970s minus 1950s responses.  
193 Descriptions of the simulations are summarized in Table 1. Each of the time slice experiments  
194 include a minimum of 50 years of data, with some including up to 100 years.

Simulation	SST and SIC Conditions	Aerosol Emission Conditions	Number of simulation Years
CTRL	HadISST 2000-2009 average	2000-2009 historical + RCP8.5	100
Ocean-Mediated Experiments			
GLOB1970	Subtract 2000s-1970s CESM1 ALL-XAER SST anomaly globally	Same as CTRL	50
GLOB1950	Subtract 2000s-1950s CESM1 ALL-XAER SST anomaly globally	Same as CTRL	50
ATL1970	Subtract 2000s-1970s SST anomaly in Atlantic and Arctic oceans and SIC anomaly in NH	Same as CTRL	50
ATL1950	Subtract 2000s-1950s SST anomaly in Atlantic and Arctic oceans and SIC anomaly in NH	Same as CTRL	50
PAC1970	Subtract 2000s-1970s SST anomaly in Pacific Ocean	Same as CTRL	50

PAC1950	Subtract 2000s-1950s SST anomaly in Pacific Ocean	Same as CTRL	50
IND1970	Subtract 2000s-1970s SST anomaly in Indian and Southern Ocean and SIC anomaly in SH	Same as CTRL	50
IND1950	Subtract 2000s-1950s SST anomaly in Indian and Southern Ocean and SIC anomaly in SH	Same as CTRL	50
Direct-Atmospheric Experiments			
GLOB1970	Same as CTRL	Set global emissions to 1970s levels	100
GLOB1950	Same as CTRL	Set global emissions to 1950s levels	100
NAMER1970	Same as CTRL	Set N American emissions to 1970s	50
NAMER1950	Same as CTRL	Set N American emissions to 1950s	50
ASIA1970	Same as CTRL	Set Asian emissions to 1970s	50
ASIA1950	Same as CTRL	Set Asian emissions to 1950s	50
EURO1970	Same as CTRL	Set European emissions to 1970s	50
EURO1950	Same as CTRL	Set European emissions to 1950s	50
AFRICA1970	Same as CTRL	Set African emissions 1970s	50
AFRICA1950	Same as CTRL	Set African emissions 1950s	50

195 Table 1: Descriptions of the SST/SIC and Aerosol emission conditions in CAM5 Atmosphere GCM  
196 simulations and their lengths.

197 We expect the combined DA and OM effects to closely approximate the aerosol-forced  
198 response seen in the CESM1 LE, and we find this to be the case despite possible errors due to the  
199 idealized nature of AGCM experiments (H2020). However, we found statistically significant  
200 non-linearity in the response for the 1970s minus 1950s, which suggests a sensitivity of the OM  
201 or DA response to background aerosol or SST conditions respectively. Unlike in (H2020), we  
202 only display the precipitation anomaly in the case of climatological background emission and

203 SST conditions for the OM and DA response, respectively. Assuming additivity between the  
204 regional effects, the sum of responses in the regional OM and DA experiments should  
205 approximate the effect of the global OM and DA responses, respectively. A more detailed  
206 discussion of the additivity can be found in Section 5.

207 In addition to evaluating the statistical significance of our results using a Student's t-test,  
208 we perform False Detection Rate (FDR) analysis of the tests in order to identify aspects of the  
209 climate response that are more robust to internal variability. Following (Wilks 2016), we select a  
210 global test threshold of 0.1, assuming high spatial correlation in seasonal average anomalies for  
211 all variables, which corresponds to an FDR threshold of about 0.05 or that approximately 5% of  
212 the tests that pass the FDR criterion are false rejections of the null hypothesis. The FDR criteria  
213 are calculated using t-test p-values from all spatial grid points globally and from all experiments  
214 in the set of all OM or all DA experiments (e.g., across all regional SST perturbation  
215 experiments), treating the set of experiments as a single set of tests.

216 The regional-averaged response is analysed using bootstrap resampling to estimate the  
217 uncertainty in the time mean anomalies. Making the standard assumption of statistical  
218 independence of individual years in the time-slice AGCM simulations, years in the simulations  
219 are randomly sampled with replacement, the time average taken, and the anomaly calculated.  
220 This is repeated  $10^5$  times to obtain a distribution which is displayed using box plots (Fig. 3i, j;  
221 Fig. 6i, j) for which the boxes represent the interquartile range, and the whiskers represent the 5-  
222 95 percentile range. For in-text averages mean anomalies are shown with 5 to 95 percentile range  
223 in brackets. Thus, a given experiment is said to result in a significant increase (decrease) if the  
224 lower (upper) whisker is above (below) zero. By resampling the mean in each simulation for a  
225 given experiment, we estimate the effect of differencing and adding multiple experiments on the  
226 uncertainty in the mean, giving a more robust estimate of the uncertainty in the sum of regional  
227 perturbation effects.

### 228 3. Regional Ocean-Mediated Results

229 The responses of African precipitation to aerosol-forced SST anomalies are shown in Fig. 3.  
230 For the 1970s minus 1950s, the global SST anomalies result in a small but significant increase in  
231 Sahel precipitation (0.18 [0.01, 0.35] mm/day) (Fig. 3a, 3i). Using the regional SST perturbation

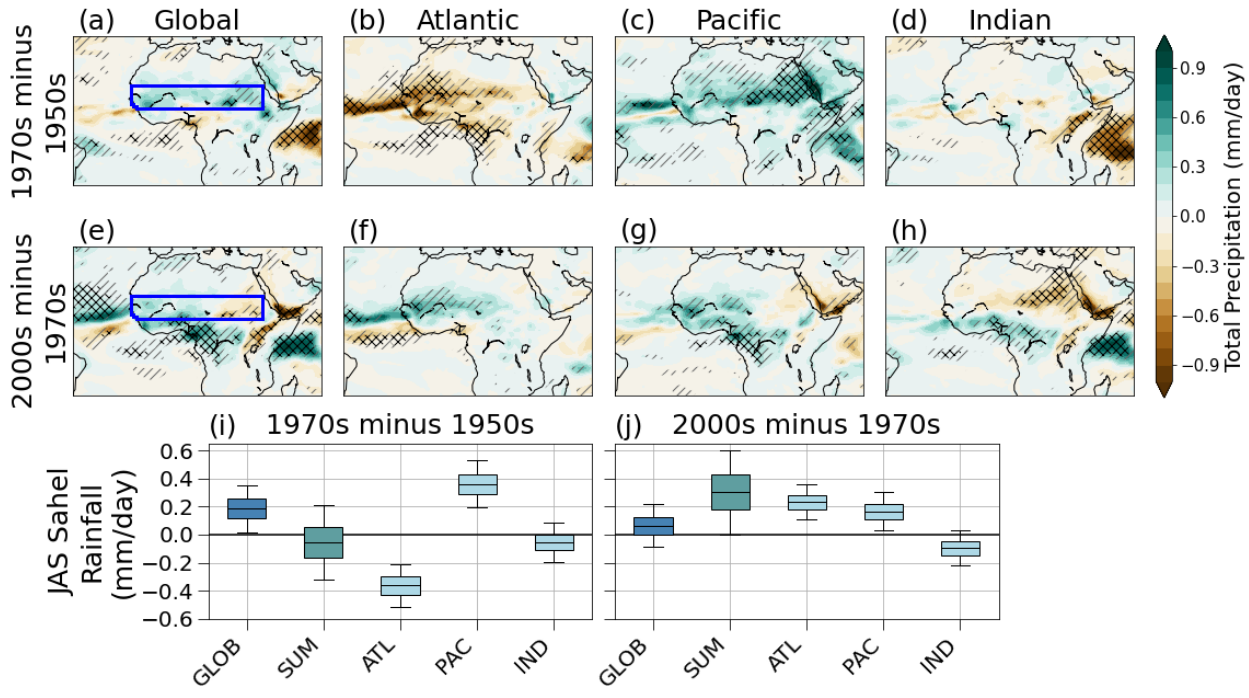


Figure 3: JAS precipitation anomaly maps from the ocean-mediated experiments for 1970s minus 1950s (top row) and 2000s minus 1970s (middle row) for the Global (a, e), Atlantic (b, f), Pacific (c, g), and Indian (d, h) SST anomalies. Single hatching indicates grid points that pass the t-test at the 95% threshold and cross hatching indicates points that additionally pass the FDR criterion ( $p_{FDR}=3.6 \times 10^{-3}$ ). The regional average anomalies (averaging region shown in blue in a, e) are shown for the 1970s minus 1950s (i) and 2000s minus 1970s (j) following the description in section 2. The SUM box displays the sum of anomalies from the ATL, PAC, and IND experiments.

232 experiments, we find that this response is a result of opposing effects of Atlantic and Pacific SST  
 233 anomalies (Figs. 3b-d). Cooling in the North Atlantic in this period reduces precipitation across  
 234 the tropical Atlantic and the Sahel (-0.36 [-0.52, -0.21]) (Fig. 3b), as expected based on the ITCZ  
 235 shift mechanism. Pacific SST cooling increases precipitation throughout the Sahel (0.36 [0.19,  
 236 0.53] mm/day), with particularly large effects in the east Sahel (Fig. 3c) and Indian SST cooling  
 237 has little effect over the Sahel during this period (-0.05 [-0.19, 0.09]) (Fig. 3d). Thus, the net OM  
 238 effect depends on the relative magnitude of Atlantic and Pacific SST effects.

239 For the 2000s minus 1970s, the global OM effect causes a weak and non-significant Sahel  
 240 precipitation increase (0.06 [-0.08, 0.22] mm/day) as a result of offsetting drying in the East  
 241 Sahel and wetting in the West and South Sahel (Fig. 3e, 3j; H2020). We find that the North  
 242 Atlantic warming caused by reduced Atlantic sector aerosol emissions in this period produces a  
 243 northward shift of the Atlantic ITCZ and a wetting signal in the west and central Sahel (0.23  
 244 [0.11, 0.36] mm/day) (Fig. 3f). Despite substantial warming in the midlatitude North Pacific,

245 Pacific SST anomalies continue to cause wetting (0.17 [0.03, 0.30] mm/day), though it is now  
 246 largest in the west Sahel (Fig. 3g). Indian ocean cooling causes drying during this period that is  
 247 marginally not significant in the regional average (-0.10 [-0.22, 0.03] mm/day). This is due to  
 248 drying in the east Sahel which is partially offset by wetting in the southwest Sahel (Fig. 3h). This  
 249 Indian OM signal appears to be the cause of the East Sahel drying in the global OM effect. We  
 250 find grid points in the Sahel that passes the FDR criterion for all OM responses except the early  
 251 period Indian ocean SST effect, indicating these portions of the response are robust to internal  
 252 variability (Fig. 3a-h).

253 The wetting response to Pacific SST cooling, particularly in the early period, suggests a  
 254 “reverse upped-ante” type response over Africa, wherein the surface cooling in the tropical  
 255 Pacific reduces diabatic heating over the region and cools the tropical troposphere globally. As  
 256 there is no corresponding cooling near the surface over Africa, this brings about a reduction in  
 257 moist stability, which in turn increases convection. This effect can be seen in the early period  
 258 zonal mean moist static energy (MSE) anomalies over Africa (Fig. 4c), where there is a MSE  
 259 decrease in the upper troposphere due to cooling. This is associated with anomalous upper-level  
 260 convergence over the Pacific and divergence over the Indian Ocean and Africa (Fig. 5c), along

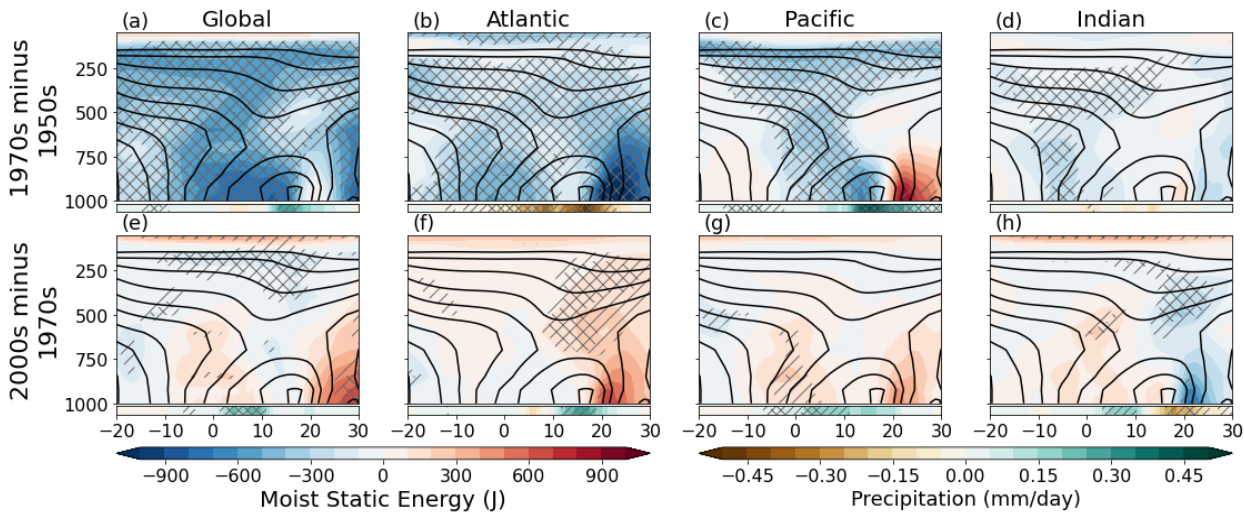


Figure 4: JAS Moist Static Energy (MSE) anomaly (filled contours) and climatology (black contours) zonally averaged over Africa (15E to 35W) of the ocean-mediated response for the 1970s minus 1950s (top row) and 2000s minus 1970s (bottom row). The zonal average precipitation anomaly is plotted in the inset along the bottom of each panel. Single hatching indicates grid points where the signal passes a t-test at 95% significance and cross hatching indicates where the grid points additionally pass the FDR criterion (MSE  $p_{FDR}=0.012$ ; Precipitation  $p_{FDR}=6.3 \times 10^{-3}$ ).

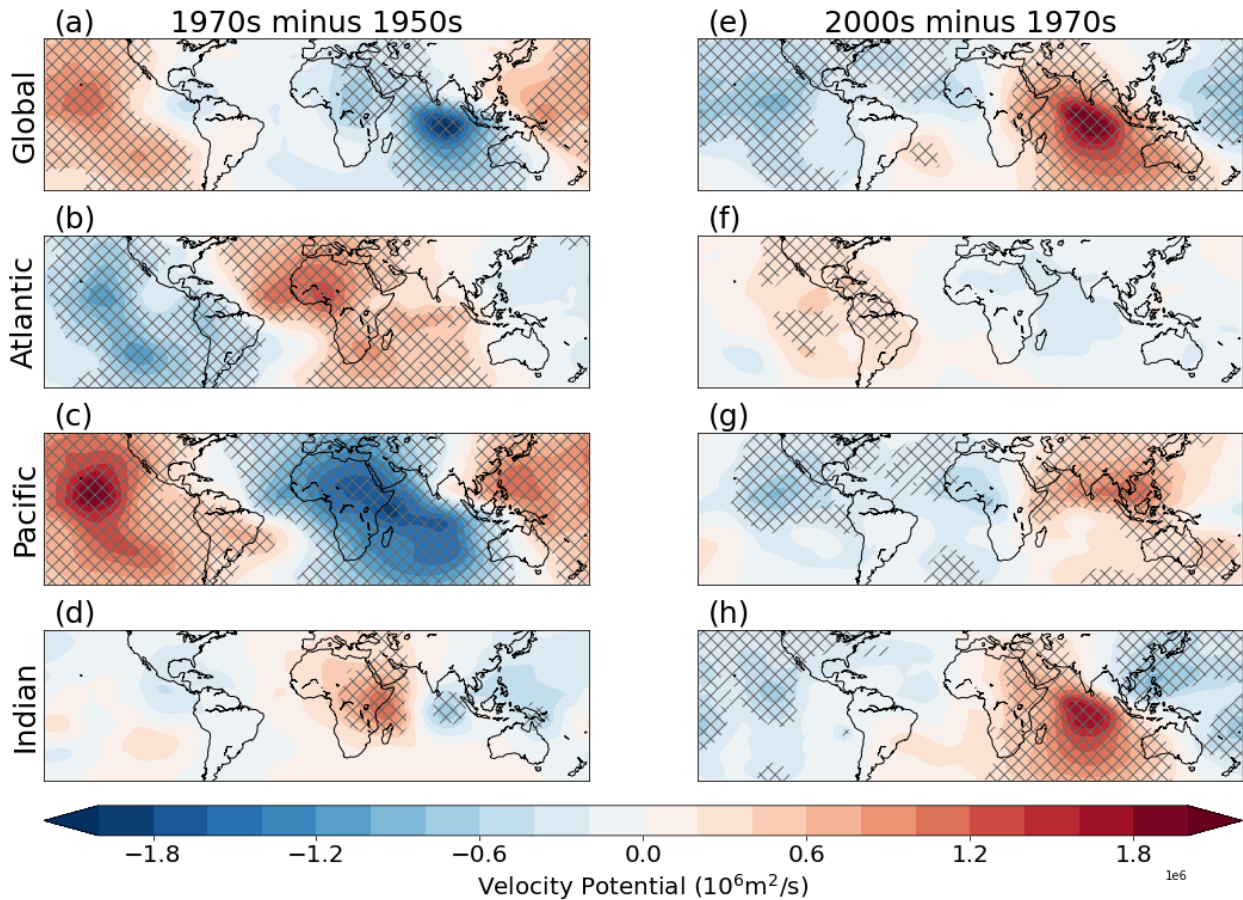


Figure 5: JAS 200hPa velocity potential anomaly due to ocean-mediated responses for the 1970s minus 1950s (left column) and 2000s minus 1970s (right column) for Global (a, e), Atlantic (b, f), Pacific (c, g), and Indian (d, h) SST anomaly effects. Single hatching indicates grid points where the response is significant at the 95% level via t-test, with cross hatching indicating grid points where the tests additionally pass the FDR criterion ( $p_{FDR}=0.04$ ).

261 with streamfunction anomalies flanking the velocity potential anomalies indicating a Walker  
 262 circulation change (not shown), which overall resembling a Gill-type response to the Pacific SST  
 263 cooling (Gill 1980; Rowell 2001). Near the surface, the local MSE maximum shifts north in  
 264 response to the aerosol-forced Pacific SST changes (Fig. 4c), in agreement with the theory that  
 265 the position of the MSE maximum and the northmost limit of the monsoon circulation are  
 266 collocated (Privé and Plumb 2007).

267 In the late period, we see continued precipitation increases due to Pacific SST anomalies  
 268 (Figs. 3g and j) despite weaker and more geographically restricted SST cooling in the basin,  
 269 including warming in the midlatitude north Pacific (Fig. 2c). We find there is no significant  
 270 upper troposphere MSE decrease in the zonal mean for this period (Fig. 4g), though there is a

271 weak but significant decline in 200hPa MSE over the east Sahel (not shown). There is a Walker  
272 circulation response with upper-level convergence over the west Pacific and Indian ocean and  
273 divergence over Africa and the East Pacific (Fig. 5g) and we posit that this is due to the  
274 continued cooling in the west Pacific, east of Asian emission regions (Fig 2c). This cooling thus  
275 influences Africa via the Walker circulation in a mechanism similar to, but weaker than, the  
276 early period response.

277 In the response to Atlantic SST anomalies, the precipitation responses follow the cooling  
278 vs. warming of the subtropical North Atlantic in the early vs. late periods. The ITCZ shifts south  
279 (north) and weakens (strengthens) corresponding to the cooling (warming) of the North Atlantic,  
280 with African monsoon precipitation following the ITCZ shifts. We see the largest MSE changes  
281 over Africa occurring to the north of the climatological MSE maximum, corresponding to the  
282 southward intensification of the MSE maximum and contraction of the monsoon circulation in  
283 the early period (Fig 4b) and a reversal of this shift in the late period (Fig. 4f). In contrast to the  
284 Pacific response, MSE anomalies for Atlantic SST change occur mainly in the lower troposphere  
285 where decreases (increases) in MSE will tend to decrease (increase) convection and thus  
286 precipitation. When this is combined with the Pacific response, we see a general MSE reduction  
287 in the tropospheric column (Fig. 4a). Thus, depending on the balance of the Pacific and Atlantic  
288 influences one may find a weak or positive JAS Sahel precipitation change despite the overall  
289 cooling of the Northern Hemisphere. Our results align with the mechanism proposed by  
290 (Giannini et al. 2013), in which the Sahel response to SST forcing is the result of a balance of  
291 effects from anomalies in the subtropical North Atlantic versus the global tropical ocean.

292 Though Indian Ocean SSTs show similar basin-wide  $-0.10\text{C}$  cooling in both periods, the  
293 early period anomalies have little effect on Africa while the late period anomalies cause  
294 significant drying in the east Sahel. We hypothesize this is due to the differing patterns of Indian  
295 Ocean cooling between the periods, which may be associated with emissions shifting from  
296 Europe to Asia. The early period cooling occurs mainly in the tropical western Indian Ocean  
297 with little change in the east (Fig. 2a). This pattern weakens the summertime north-south SST  
298 gradient in the Indian ocean increases Sahel precipitation, while overall mean cooling signal  
299 causes drying (Chung and Ramanathan 2006; Dyer et al. 2017). This causes upper-level  
300 convergence over east Africa and divergence over the east Indian ocean (Fig. 5d), resulting in

301 drying over parts of east Africa but has little effect on the Sahel. For the late period, the pattern  
 302 of Indian Ocean cooling differs from the previous period, with cooling being focused near the  
 303 equator and in the central and east Indian Ocean. This results in a positive north-south gradient  
 304 anomaly which along with the overall cooling both tend to cause drying in the East Sahel (Chung  
 305 and Ramanathan 2006; Dyer et al. 2017). This is associated with an upper-level convergence  
 306 anomaly that covers much of the Indian Ocean and East Africa and divergence over the Pacific  
 307 and weak divergence anomalies over the North Atlantic (Fig. 5h).

### 308 4. Regional Direct-Atmospheric Response

309 For the 1970s minus 1950s, global emission change causes drying in the Sahel (-0.20 [-0.31, -  
 310 0.09] mm/day) (Fig. 6a). This is the result of a combination of effects from all emission regions  
 311 as the sum of the regional emissions responses is a statistically significant drying (-0.38 [-0.72, -  
 312 0.03] mm/day), which is consistent with the global emission effect (Fig 6i). However, only North

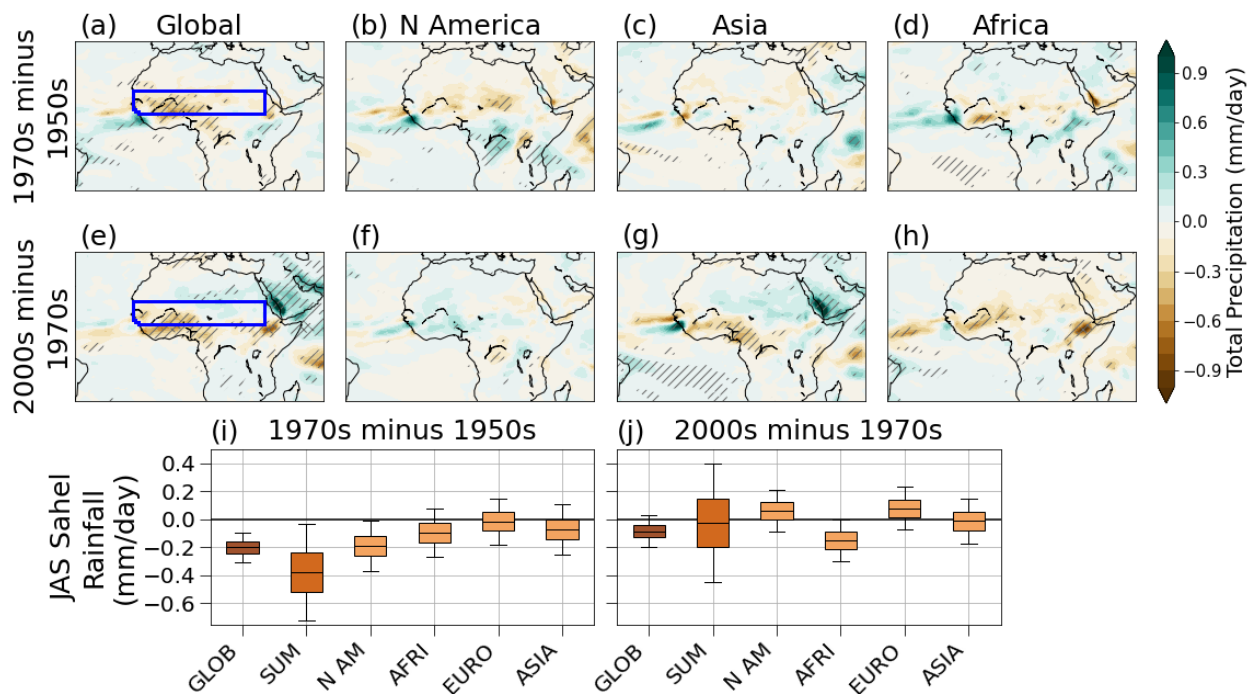


Figure 6: JAS precipitation anomaly maps from the direct-atmospheric experiments for 1970s minus 1950s (top row) and 2000s minus 1970s (middle row) for the Global (a, e), North America (b, f), Asian (c, g), and African (d, h) emission changes. Single hatching indicates grid points that pass the t-test at the 95% threshold and cross hatching indicates points that additionally pass the FDR criterion ( $p_{FDR}=9 \times 10^{-5}$ ). The regional average anomalies (averaging region shown in blue in a, e) are shown for the 1970s minus 1950s (i) and 2000s minus 1970s (j) following the description in section 2. The SUM box displays the sum of anomalies from the N AM, AFRI, EURO, and ASIA experiments.

313 American emission changes cause significant drying ( $-0.19$  [ $-0.37, -0.01$ ] mm/day) (Fig 6i),  
 314 which mainly occurs in the East Sahel (Fig. 6b). For the 2000s minus 1970s, the global emission  
 315 effect causes some non-significant drying in the Sahel ( $-0.08$  [ $-0.20, 0.03$ ] mm/day), along with  
 316 drying in the Gulf of Guinea region (Fig. 6e). Drying in the Sahel is mainly due to African  
 317 emission increases which cause a statistically significant drying ( $-0.15$  [ $-0.30, 0.0$ ] mm/day) (Fig.  
 318 6h, j). Asian emission increases have little effect on the Sahel ( $-0.01$  [ $-0.17, 0.15$ ] mm/day) but  
 319 are the main cause of the drying effect in the Gulf of Guinea and Central Africa regions (Fig 6g).  
 320 The sum of these effects is a weak anomaly in the Sahel ( $-0.03$  [ $-0.45, 0.39$ ] mm/day) (Fig. 6j).  
 321 In the spatial maps, some experiments result in precipitation responses that are significant at the  
 322 95% level in Africa, however only late period African emissions result in FDR significant  
 323 anomalies which occur in the Ethiopian Highlands (Fig. 6h). Thus, the DA precipitation  
 324 responses have a lower signal to noise than the OM responses. The DA Sahel drying effect of  
 325 North American emissions in this period indicates that the CESM1 Sahel wetting signal in  
 326 response to decreasing United States SO<sub>2</sub> emissions found by Westervelt et al., 2017 is not  
 327 entirely driven via the hemispheric temperature responses, but is also partly DA.

328 Despite European emissions being the primary source of sulphate burden changes in  
 329 northern Africa (and the Sahel) in both periods (Fig. 1c, d – purple contours), we find that they

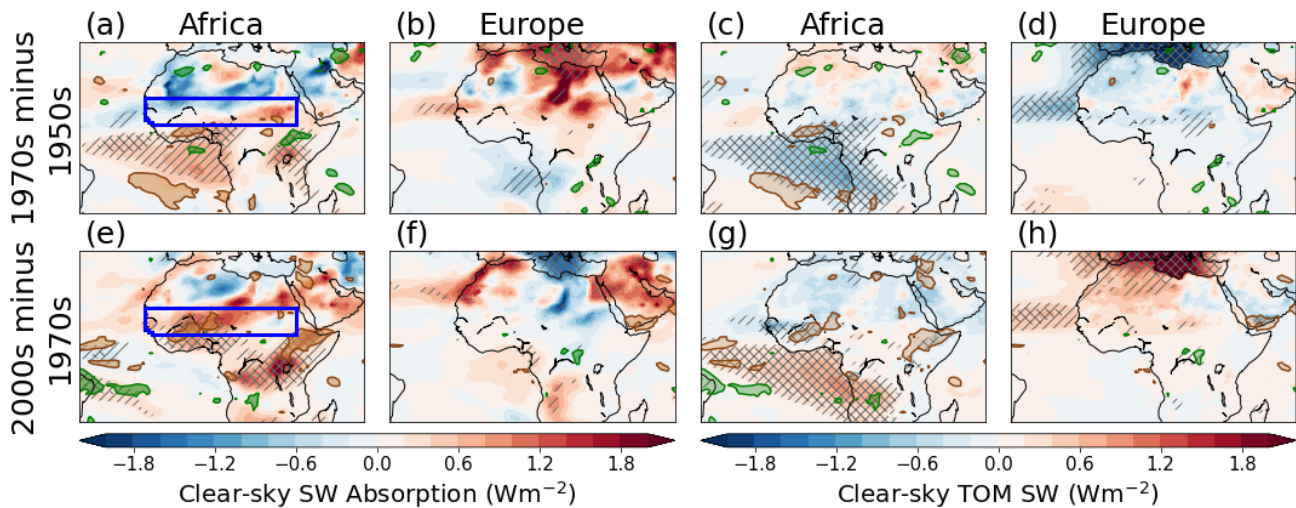


Figure 7: Clear-sky atmospheric SW absorption shortwave anomalies (a, b, e, f) and Clear-sky Top of Model (TOM) (c, d, g, h) for the African (1970s minus 1950s: a and c; 2000s minus 1970s: e and g) and European (1970s minus 1950s: b and d; 2000s minus 1970s: f and h) emission change simulations. Hatching indicates regions of statistical significance, while cross hatching indicates regions that additionally pass the FDR criterion. Grid points in which there are statistically significant ( $p < 0.05$ ) drying (brown) or wetting (green) signals are shown in contours.

330 have little effect on Sahel precipitation in either period (Fig. 6i, j). This appears to be due to  
331 weak direct aerosol radiative forcing as indicated by relatively weak anomalies in top-of-model  
332 (TOM) clear-sky net shortwave anomalies over land in North Africa in both periods (Fig. 7d, h).  
333 The weak direct forcing may be due to the high background albedo and aerosol concentrations of  
334 the Sahara, as clear-sky shortwave anomalies are stronger over the subtropical Atlantic off the  
335 coast of Africa than adjacent land regions, despite similar sulphate burden changes (Fig. 2b).  
336 This differs from the previous study by (Dong et al. 2014) wherein it was found that increasing  
337 European sulphate emissions caused DA drying in the Sahel. But this result is consistent with the  
338 lack of a DA effect in CAM5 in response to a 10x increase in European sulphate emissions  
339 shown in (Liu et al. 2018). Thus, it appears the strength of the European sulphate emission DA  
340 drying effect is model dependent.

341         The largest contributor to the DA effect in the early period is North American emission  
342 changes. However, these emission changes have a minimal impact on North African aerosol  
343 burdens (Fig. 2b, S1a) and SW forcing (Fig. S5a, c). Thus, the DA effect of North American  
344 emissions appears to be a remote circulation response, mediated through circulation changes  
345 over the North Atlantic (Fig. S4a, e). African emissions also cause drying, though this mainly  
346 occurs in coastal regions of West Africa. This is the result of SW forcing in the coastal and  
347 tropical regions of Africa (Fig. 7a, c).

348         In the late period, the two main DA influences on West Africa come from Asian  
349 emissions, which cause drying in coastal West Africa, and from African emissions, which cause  
350 drying in the West Sahel. The Asian emission response seen here is consistent with the DA  
351 drying signal found in (Dong et al. 2014) and disagrees with the multi-model mean DA sulphate  
352 effect of (Liu et al. 2018), but has a similar pattern of response to the CAM5 experiment shown  
353 therein. Thus, it appears that the Asian DA effect is predominantly driven by sulphate cooling of  
354 Asian land regions which shifts Asian monsoon circulation, causing anomalous upper-level  
355 divergence (Fig. Td) and upper tropospheric warming over the Indian ocean. This warming  
356 signal spreads over the tropical upper troposphere, inducing a Walker circulation adjustment  
357 with upper-level convergence (Fig. S4d) and drying effects over West Africa. Local African  
358 emissions result in increases in black carbon burden across Africa and sulphate burden over West  
359 Sahel in this period (Fig. 2d; Fig S1b). This results in a decrease in TOM clear-sky SW and

360 increase in SW absorption over West Africa (Fig. 7f, h) which both contribute to the drying  
361 signal. The TOM SW forcing by radiative cooling induced subsidence (Dong et al., 2015) and  
362 the SW absorption by warming and stabilizing the troposphere (Andrews et al. 2010; Samset et  
363 al. 2016). The SW atmospheric absorption anomalies in West Africa are largely collocated with  
364 the precipitation response (Fig. 7e), while the strongest TOM SW anomalies occur to the west of  
365 the drying signal (Fig. 7g). This suggests absorbing aerosols may be the principal cause of the  
366 drying effect.

## 367 5. Additivity in Regional Simulations

368 As noted in section 2, given the design of the regional SST and emission experiments, we  
369 expect the sum of the regional SST and emission experiments responses to approximate the  
370 global OM and DA responses respectively. For the regional OM responses, we find that the sum  
371 of regional SST precipitation responses differs from the global OM effect in both periods, with  
372 the sum drying (-0.06 [-0.32, 0.21] mm/day) as opposed to wetting (0.18 [0.01, 0.35] mm/day) in  
373 the early period (Fig. S3c, d) and a much stronger wetting (0.31 [0, 0.61] mm/day) than the  
374 global SST effect (0.06 [-0.08, 0.22] mm/day) in the later period (Fig. S3g, h). However, while  
375 the differences are substantial, they are statistically non-significant due to the high level of noise  
376 introduced by adding together experiments (Fig. S3d, h). This is more clearly demonstrated by  
377 the sum box plots in Fig. 3i and 3j wherein we find the mean global OM response in the Sahel  
378 falls within the 5-95 percentile range of bootstrap resampled sum responses in both periods,  
379 despite opposite signed mean responses in the early period. Thus, it is not possible to ascertain  
380 whether there are significant nonlinearities in the response. However, analysis of the 200hPa  
381 velocity potential, which has greater signal to noise, shows similar patterns of response in the  
382 sum and global OM responses with no significant non-additivity (Fig. S6). Key features are  
383 captured such as the cancellation of early period Atlantic and Pacific OM responses over the  
384 Atlantic/Africa (Fig. S6c), which corresponds to the weak global OM velocity potential response  
385 over those regions (Fig. S6a). Similar additivity across the OM simulations is also seen in the  
386 zonally averaged MSE response over Africa (not shown), suggesting that large scale atmospheric  
387 responses to OM can be reasonably attributed to responses from different ocean basins.

388 In the regional emission and global DA response case, we again find differences in  
389 precipitation response between the sum of regional emission experiments and the global DA

390 response (Fig. S3a, e), though the agreement in sign and pattern is better compared to the sum of  
391 OM responses. In both periods, the spread of mean values in the global emission simulations lies  
392 entirely within the wide spread of the uncertainty in the regional sum (Fig. 6i, j). Thus, we  
393 cannot ascertain if the emissions regions we have not tested have an important role in explaining  
394 the residual or if there are nonlinear effects. Comparing the 200hPa velocity potential responses,  
395 we find less agreement than in the OM sum case, with differences in both periods, particularly  
396 over the Pacific (Fig. S7). However, these velocity potential responses have lower signal-to-  
397 noise than the OM responses. Nevertheless, the sign of the response is consistent over Africa.  
398 Thus, while there are apparent differences between the sum of regional effects and the global  
399 effect for both OM and DA and for both periods, the noise introduced by the summation renders  
400 it difficult to determine if these are statistically significant non-additive signals, particularly for  
401 noisy variables such as precipitation.

## 402 6. Conclusions

403 In our previous work (H2020) we found that for the 1970s minus 1950s the OM component of  
404 the Sahel response to aerosol forcing resulted in a weak increase in precipitation with the DA  
405 component causing most of the drying. For the 2000s minus 1970s, we found that the OM effect  
406 increases Sahel precipitation while the DA effect continues to cause drying. However, these  
407 simulations were not able to resolve the question of why OM response resulted in increased  
408 Sahel precipitation despite substantial cooling in the North Atlantic for the early period, and why  
409 the DA response continued to cause drying in spite of large declines in sulphate burdens over  
410 North Africa for the late period. To address these questions, we have regionally decomposed the  
411 DA and OM effects in CAM5. Using time-slice AGCM simulations, we identified the regional  
412 OM response by applying aerosol-induced SST anomalies in different basins and the regional  
413 DA response by changing aerosol emissions in different regions. In doing so, we gain insight  
414 into the mechanisms driving the aerosol-forced influence on Sahel climate and find that the  
415 pattern of SST and emission change is crucial for dictating the overall response.

416 We find that the aerosol-forced OM response is principally determined by the balance of  
417 Atlantic and tropical Pacific SST anomaly effects, with additional modulating effects due to  
418 Indian Ocean anomalies. Due to changing European and North American emissions, North  
419 Atlantic SST anomalies switch sign between the early and late periods, changing the Atlantic

420 SST effect from Sahel drying to wetting. Pacific SST also undergo multidecadal variations, but  
421 there is cooling in the tropical West Pacific in both periods, which drives Sahel wetting. Thus,  
422 the two basins have opposing effects in the early period, with the Pacific induced wetting  
423 overwhelming the North Atlantic induced drying, and complementary effects in the later period,  
424 causing wetting. Indian ocean cooling has little effect in the early period, but causes drying in the  
425 late period, possibly because of a change in the sign of the north-south gradient in SST  
426 anomalies.

427         The aerosol DA drying in the Sahel is the result of emissions from different regions in the  
428 two periods. Early period drying is predominantly due to North American emissions, while later  
429 period drying is due to local African emissions. Asian emissions cause drying in the Gulf of  
430 Guinea region via atmospheric circulation adjustments. Notably, there is a weak response to  
431 European emission changes in both periods, despite the bulk of North African aerosol burden  
432 anomalies being linked to European emissions. Comparing our results to those of Liu et al.,  
433 2018, we find that our European and Asian emission responses are similar to the annual mean  
434 responses in regional 10x sulphate experiments for CAM5 but differ in sign from the multi-  
435 model mean. This suggests there is substantial inter-model uncertainty in the DA effect of  
436 regional aerosol emissions on the Sahel. The discrepancy between CAM5 and the rest of the  
437 PDRMIP ensemble may be due to the unusually strong aerosol-cloud radiative forcing in the  
438 model, as CAM5 was one of two models with prognostic aerosol and both indirect effects in the  
439 ensemble (Liu et al. 2018).

440         As this study uses AGCM simulations, these experiments are idealized and may be  
441 affected by errors such as those arising from the lack of ocean-atmosphere coupling, the use of  
442 time-slice rather than transient forcing, and differences in the background SST/SIC state. In the  
443 global DA and OM experiments, we find there is statistically significant non-additivity in the  
444 early period Sahel precipitation response (Fig. 12 in (H2020)) arising from dependence on the  
445 background state. Such background dependence suggests that the response to aerosol forcing  
446 may also depend on the level of background GHG forcing (e.g. Deng et al. 2020), though such  
447 non-linearity is not detectable in the CESM1 LE Sahel mean JAS precipitation (H2020). As the  
448 GHG concentrations and the background SST are set to 2000s levels, the baseline climate is  
449 warmer than the climate in the historical LE experiments, which may change the DA effect due

450 to increased cloud cover and aerosol deposition under warmer conditions (Feichter et al. 2004). It  
451 also likely impacts the response to regional perturbations, though we have not tested that here.  
452 We find that the sum of the regional perturbation responses often differs substantially from the  
453 global perturbation response, even differing in sign in the case of the early period OM response.  
454 However, these differences are not statistically significant due to the noise in each experiment  
455 being compounded together when calculating the sum, resulting in large uncertainties. This also  
456 means we are not able to assess with confidence the impact of the emission regions we did not  
457 include among our DA experiments. Using FDR testing, we assess the statistical robustness of  
458 our results and find that the OM responses are quite robust to internal variability in Africa, while  
459 the DA responses are less so.

460 As we find substantial effects of the DA response and remote effects of Pacific and  
461 Indian Ocean SST on Sahel precipitation, the effect of aerosol forcing on the Sahel in a coupled  
462 system therefore cannot be simply interpreted as a response to the Atlantic hemispheric SST  
463 differential. Furthermore, the fact that many of the regional perturbation results change sign and  
464 magnitude between the two periods underscores the need to consider the transient response when  
465 assessing the aerosol influence on historical climate (and motivates the use of large ensembles  
466 which allow the confident assessment of forced signals on multidecadal timescales (Deser et al.  
467 2020)). Thus, care should be taken when interpreting correlations between forced signals in  
468 coupled system, as they may covary simply due to their shared forcing and proximate drivers are  
469 modulated by remote effects.

## 470 Acknowledgements

471 We thank the reviewers for their constructive comments on this manuscript. This work  
472 was supported by funding from Environment and Climate Change Canada and the National  
473 Science and Engineering Research Council of Canada. Computations were performed on the  
474 Niagara supercomputer at the SciNet HPC Consortium. SciNet is funded by the Canada  
475 Foundation for Innovation; the Government of Ontario; Ontario Research Fund - Research  
476 Excellence; and the University of Toronto.

477 This material is based in part on work supported by the National Center for Atmospheric  
478 Research, which is a major facility sponsored by the National Science Foundation (NSF) under  
479 Cooperative Agreement 1852977. CESM1 LE data are available from ESG at

480 <http://www.cesm.ucar.edu/projects/communityprojects/LENS/datasets.html>. The CESM project  
481 is supported primarily by the NSF.

## 482 Data Availability

483 The data used for the results shown in this work can be found at: Hirasawa, Haruki; Kusher, Paul  
484 J.; Sigmond, Michael; Fyfe, John; Deser, Clara, 2021, "Data for: Evolving Sahel rainfall  
485 response to anthropogenic aerosols driven by shifting regional oceanic and emission influences",  
486 <https://doi.org/10.5683/SP3/1ZGHXA>, Scholars Portal Dataverse, DRAFT VERSION

## 487 7. References

- 488 Ackerley, D., B. B. Booth, S. H. E. Knight, E. J. Highwood, D. J. Frame, M. R. Allen, and D. P.  
489 Rowell, 2011: Sensitivity of Twentieth-Century Sahel rainfall to sulfate aerosol and CO<sub>2</sub>  
490 forcing. *Journal of Climate*, **24**, 4999–5014, <https://doi.org/10.1175/JCLI-D-11-00019.1>.
- 491 Andrews, T., P. M. Forster, O. Boucher, N. Bellouin, and A. Jones, 2010: Precipitation, radiative  
492 forcing and global temperature change. *Geophysical Research Letters*, **37**,  
493 <https://doi.org/10.1029/2010GL043991>.
- 494 Biasutti, M., 2013: Forced Sahel rainfall trends in the CMIP5 archive. *Journal of Geophysical*  
495 *Research Atmospheres*, **118**, 1613–1623, <https://doi.org/10.1002/jgrd.50206>.
- 496 —, 2019: Rainfall trends in the African Sahel: Characteristics, processes, and causes. *Wiley*  
497 *Interdisciplinary Reviews: Climate Change*, **10**, 1–22, <https://doi.org/10.1002/wcc.591>.
- 498 —, I. M. Held, A. H. Sobel, and A. Giannini, 2008: SST forcings and Sahel rainfall variability in  
499 simulations of the twentieth and twenty-first centuries. *Journal of Climate*, **21**, 3471–3486,  
500 <https://doi.org/10.1175/2007JCLI1896.1>.
- 501 Charney, J. G., 1975: Dynamics of deserts and drought in the Sahel. *Quarterly Journal of the*  
502 *Royal Meteorological Society*, **101**, 193–202, <https://doi.org/10.1002/qj.49710142802>.
- 503 Chou, C., and J. D. Neelin, 2004: Mechanisms of Global Warming Impacts on Regional Tropical  
504 Precipitation. *Journal of Climate*, **17**.
- 505 Chung, C. E., and V. Ramanathan, 2006: Weakening of north Indian SST gradients and the  
506 monsoon rainfall in India and the Sahel. *Journal of Climate*, **19**, 2036–2045,  
507 <https://doi.org/10.1175/JCLI3820.1>.
- 508 Deng, J., A. Dai, and H. Xu, 2020: Nonlinear Climate Responses to Increasing CO<sub>2</sub> and  
509 Anthropogenic Aerosols Simulated by CESM1. *Journal of Climate*, **33**, 281–301,  
510 <https://doi.org/10.1175/jcli-d-19-0195.1>.

511 Deser, C., A. S. Phillips, I. R. Simpson, N. Rosenbloom, D. Coleman, and S. Stevenson, 2020:  
512 Isolating the Evolving Contributions of Anthropogenic Aerosols and Greenhouse Gases: A  
513 New CESM1 Large Ensemble Community Resource. *Journal of Climate*, 1–61.

514 Dong, B., and R. Sutton, 2015: Dominant role of greenhouse-gas forcing in the recovery of Sahel  
515 rainfall. *Nature Climate Change*, **5**, 757–760, <https://doi.org/10.1038/nclimate2664>.

516 —, R. T. Sutton, E. Highwood, and L. Wilcox, 2014: The impacts of European and Asian  
517 anthropogenic sulfur dioxide emissions on Sahel rainfall. *Journal of Climate*, **27**, 7000–  
518 7017, <https://doi.org/10.1175/JCLI-D-13-00769.1>.

519 Dyer, E. L. E., D. B. A. Jones, R. Li, H. Sawaoka, and L. Mudryk, 2017: Sahel precipitation and  
520 regional teleconnections with the Indian Ocean. *Journal of Geophysical Research*, **122**,  
521 5654–5676, <https://doi.org/10.1002/2016JD026014>.

522 Feichter, J., E. Roeckner, U. Lohmann, and B. Liepert, 2004: Nonlinear aspects of the climate  
523 response to Greenhouse gas and aerosol forcing. *Journal of Climate*, **17**, 2384–2398,  
524 [https://doi.org/10.1175/1520-0442\(2004\)017<2384:NAOTCR>2.0.CO;2](https://doi.org/10.1175/1520-0442(2004)017<2384:NAOTCR>2.0.CO;2).

525 Folland, C. K., T. N. Palmer, and D. E. Parker, 1986: Sahel rainfall and worldwide sea  
526 temperatures, 1901-85. *Nature*, **320**, 602–607, <https://doi.org/10.1038/320602a0>.

527 Gaetani, M., G. Messori, Q. Zhang, C. Flamant, and F. S. R. Pausata, 2017: Understanding the  
528 mechanisms behind the northward extension of the West African monsoon during the  
529 mid-holocene. *Journal of Climate*, **30**, 7621–7642, <https://doi.org/10.1175/JCLI-D-16-0299.1>.

531 Giannini, A., and A. Kaplan, 2019: The role of aerosols and greenhouse gases in Sahel drought  
532 and recovery. *Climatic Change*, **152**, 449–466, <https://doi.org/10.1007/s10584-018-2341-9>.

533

534 —, M. Biasutti, I. M. Held, and A. H. Sobel, 2008: A global perspective on African climate.  
535 *Climatic Change*, **90**, 359–383, <https://doi.org/10.1007/s10584-008-9396-y>.

536 Giannini, A., S. Salack, T. Lodoun, A. Ali, A. T. Gaye, and O. Ndiaye, 2013: A unifying view of  
537 climate change in the Sahel linking intra-seasonal, interannual and longer time scales.  
538 *Environmental Research Letters*, **8**, <https://doi.org/10.1088/1748-9326/8/2/024010>.

539 Gill, A. E., 1980: Some simple solutions for heat-induced tropical circulation. *Quarterly Journal*  
540 *of the Royal Meteorological Society*, **106**, 447–462,  
541 <https://doi.org/10.1002/qj.49710644905>.

542 Held, I. M., T. L. Delworth, J. Lu, K. L. Findell, and T. R. Knutson, 2005: Simulation of Sahel  
543 drought in the 20th and 21st centuries. *Proceedings of the National Academy of Sciences of*  
544 *the United States of America*, **102**, 17891–17896,  
545 <https://doi.org/10.1073/pnas.0509057102>.

546 Herman, R. J., A. Giannini, M. Biasutti, and Y. Kushnir, 2020: The effects of anthropogenic and  
547 volcanic aerosols and greenhouse gases on twentieth century Sahel precipitation. *Scientific*  
548 *Reports*, **10**, 1–11, <https://doi.org/10.1038/s41598-020-68356-w>.

549 Hirasawa, H., P. J. Kushner, M. Sigmond, J. Fyfe, and C. Deser, 2020: Anthropogenic aerosols  
550 dominate forced multidecadal Sahel precipitation change through distinct atmospheric and  
551 oceanic drivers. *Journal of Climate*, **33**, 10187–10204, [https://doi.org/10.1175/JCLI-D-19-](https://doi.org/10.1175/JCLI-D-19-0829.1)  
552 [0829.1](https://doi.org/10.1175/JCLI-D-19-0829.1).

553 Hua, W., A. Dai, L. Zhou, M. Qin, and H. Chen, 2019: An Externally Forced Decadal Rainfall  
554 Seesaw Pattern Over the Sahel and Southeast Amazon. *Geophysical Research Letters*, **46**,  
555 923–932, <https://doi.org/10.1029/2018GL081406>.

556 Hurrell, J. W., J. J. Hack, D. Shea, J. M. Caron, and J. Rosinski, 2008: A new sea surface  
557 temperature and sea ice boundary dataset for the community atmosphere model. *Journal*  
558 *of Climate*, **21**, 5145–5153, <https://doi.org/10.1175/2008JCLI2292.1>.

559 Hwang, Y. T., D. M. W. Frierson, and S. M. Kang, 2013: Anthropogenic sulfate aerosol and the  
560 southward shift of tropical precipitation in the late 20th century. *Geophysical Research*  
561 *Letters*, **40**, 2845–2850, <https://doi.org/10.1002/grl.50502>.

562 Kang, S. M., S. Xie, C. Deser, and B. Xiang, 2021: Zonal mean and shift modes of historical  
563 climate response to evolving aerosol distribution. *Science Bulletin*,  
564 <https://doi.org/10.1016/j.scib.2021.07.013>.

565 Kawase, H., M. Abe, Y. Yamada, T. Takemura, T. Yokohata, and T. Nozawa, 2010: Physical  
566 mechanism of long-term drying trend over tropical North Africa. *Geophysical Research*  
567 *Letters*, **37**, L09706, <https://doi.org/10.1029/2010GL043038>.

568 Liu, L., and Coauthors, 2018: A PDRMIP Multimodel study on the impacts of regional aerosol  
569 forcings on global and regional precipitation. *Journal of Climate*, **31**, 4429–4447,  
570 <https://doi.org/10.1175/JCLI-D-17-0439.1>.

571 Liu, X., and Coauthors, 2012: Toward a minimal representation of aerosols in climate models:  
572 Description and evaluation in the Community Atmosphere Model CAM5. *Geoscientific*  
573 *Model Development*, **5**, 709–739, <https://doi.org/10.5194/gmd-5-709-2012>.

574 Lu, J., 2009: The dynamics of the Indian Ocean sea surface temperature forcing of Sahel  
575 drought. *Climate Dynamics*, **33**, 445–460, <https://doi.org/10.1007/s00382-009-0596-6>.

576 Malavelle, F. F., and Coauthors, 2017: Strong constraints on aerosol-cloud interactions from  
577 volcanic eruptions. *Nature*, **546**, 485–491, <https://doi.org/10.1038/nature22974>.

578 Mohino, E., S. Janicot, and J. Bader, 2011: Sahel rainfall and decadal to multi-decadal sea  
579 surface temperature variability. *Climate Dynamics*, **37**, 419–440,  
580 <https://doi.org/10.1007/s00382-010-0867-2>.

581 Myhre, G., and Coauthors, 2017: PDRMIP: A precipitation driver and response model  
582 intercomparison project-protocol and preliminary results. *Bulletin of the American*  
583 *Meteorological Society*, **98**, 1185–1198, <https://doi.org/10.1175/BAMS-D-16-0019.1>.

584 Neale, R. B., and Coauthors, 2012: *Description of the NCAR Community Atmosphere Model*  
585 *(CAM 5.0)*. 1–274 pp.

586 Pausata, F. S. R., G. Messori, and Q. Zhang, 2016: Impacts of dust reduction on the northward  
587 expansion of the African monsoon during the Green Sahara period. *Earth and Planetary*  
588 *Science Letters*, **434**, 298–307, <https://doi.org/10.1016/j.epsl.2015.11.049>.

589 Privé, N. C., and A. R. Plumb, 2007: Monsoon dynamics with interactive forcing. Part I:  
590 Axisymmetric studies. *Journal of the Atmospheric Sciences*, **64**, 1417–1430,  
591 <https://doi.org/10.1175/JAS3916.1>.

592 Rodríguez-Fonseca, B., and Coauthors, 2011: Interannual and decadal SST-forced responses of  
593 the West African monsoon. *Atmospheric Science Letters*, **12**, 67–74,  
594 <https://doi.org/10.1002/asl.308>.

595 Rotstayn, L. D., and U. Lohmann, 2002: Tropical Rainfall Trends and the Indirect Aerosol Effect.  
596 *Journal of Climate*, **15**, 2103–2116, [https://doi.org/10.1175/1520-](https://doi.org/10.1175/1520-0442(2002)015<2103:TRTATI>2.0.CO;2)  
597 [0442\(2002\)015<2103:TRTATI>2.0.CO;2](https://doi.org/10.1175/1520-0442(2002)015<2103:TRTATI>2.0.CO;2).

598 Rowell, D. P., 2001: Teleconnections between the tropical Pacific and the Sahel. *Quarterly*  
599 *Journal of the Royal Meteorological Society*, **127**, 1683–1706,  
600 <https://doi.org/10.1256/smsqj.57511>.

601 Samset, B. H., and Coauthors, 2016: Fast and slow precipitation responses to individual climate  
602 forcers: A PDRMIP multimodel study. *Geophysical Research Letters*, **43**, 2782–2791,  
603 <https://doi.org/10.1002/2016GL068064>.

604 Smith, S. J., J. van Aardenne, Z. Klimont, R. J. Andres, A. Volke, and S. Delgado Arias, 2011:  
605 Anthropogenic sulfur dioxide emissions: 1850–2005. *Atmospheric Chemistry and Physics*,  
606 **11**, 1101–1116, <https://doi.org/10.5194/acp-11-1101-2011>.

607 Toll, V., M. Christensen, J. Quaas, and N. Bellouin, 2019: Weak average liquid-cloud-water  
608 response to anthropogenic aerosols. *Nature*, **572**, 51–55, [https://doi.org/10.1038/s41586-](https://doi.org/10.1038/s41586-019-1423-9)  
609 [019-1423-9](https://doi.org/10.1038/s41586-019-1423-9).

610 Undorf, S., M. A. Bollasina, and G. C. Hegerl, 2018: Impacts of the 1900–74 increase in  
611 anthropogenic aerosol emissions from North America and Europe on Eurasian summer  
612 climate. *Journal of Climate*, **31**, 8381–8399, <https://doi.org/10.1175/JCLI-D-17-0850.1>.

613 Wang, C., 2015: Anthropogenic aerosols and the distribution of past large-scale precipitation  
614 change. *Geophysical Research Letters*, **42**, 10876–10884,  
615 <https://doi.org/10.1002/2015GL066416>.

616 Westervelt, D. M., and Coauthors, 2017: Multimodel precipitation responses to removal of U.S.  
617 sulfur dioxide emissions. *Journal of Geophysical Research*, **122**, 5024–5038,  
618 <https://doi.org/10.1002/2017JD026756>.

619 Wilks, D. S., 2016: “The stippling shows statistically significant grid points”: How research  
620 results are routinely overstated and overinterpreted, and what to do about it. *Bulletin of*  
621 *the American Meteorological Society*, **97**, 2263–2273, [https://doi.org/10.1175/BAMS-D-15-](https://doi.org/10.1175/BAMS-D-15-00267.1)  
622 [00267.1](https://doi.org/10.1175/BAMS-D-15-00267.1).

623 Zelinka, M. D., T. Andrews, P. M. Forster, and K. E. Taylor, 2014: Quantifying components of  
624 aerosol-cloud-radiation interactions in climate models. *Journal of Geophysical Research:*  
625 *Atmospheres*, **119**, 7599–7615, <https://doi.org/10.1002/2014JD021710>.

626

627